Electrode Configuration with Howland Current Source and Demodulator for Electrical Impedance Tomography

Hossein Nasiri [*,1] **Rafael Benetti** [*,2] **Rogério Y. Takimoto** [*,3]
André C. M. Cavalheiro [*,4] **Guilherme C. Duran** [*,5]
Thiago C. Martins [*,6] **Marcos S. G. Tsuzuki** [*,7]

[*] *Laboratory of Computational Geometry*
Mechatronics and Mechanical Systems Engineering Department,
Escola Politécnica da Universidade de São Paulo, São Paulo, Brazil

Abstract: Electrical Impedance Tomography (EIT) uses boundary voltage measurements due to multiple injection current patterns to reconstruct cross-sectional impedance images. Usually, the hardware does not provide any capacitive information and the reconstructed image is only based on conductivity. An approach where each electrode has its own Howland current source is a powerful and innovative architecture in which different current injections can be implemented. However, the potential source of error increases with this new architecture when compared with conventional architectures. This paper enumerates some of the potential errors considering the main modules of the electrode: 1. Howland current source; 2. ADC and DAC converters; and 3. The demodulator. A methodology for verifying ADC and DAC precision and linearity is proposed.

Keywords: signal processing, electrical impedance tomography, demodulator.

1. INTRODUCTION

Electrical Impedance Tomography (EIT) is a noninvasive imaging modality for obtaining conductivity images of the interior of an object, which are inferred from the electrical potential measurements taken at the object's boundary. This technique consists of converting a physical property of the object, its electrical conductivity distribution, into a grey scale value, so that it can then be rendered as an image. As long as there is no access to the interior of the body, the conductivity distribution must be inferred from electrical potential measurements taken on the surface of the body. The image can be reconstructed as an optimization problem, for example, using simulated annealing (Martins and Tsuzuki, 2011, 2012, 2013, 2015, 2017). Recently, artificial neural networks have also been used (Bianchessi et al., 2020).

Usually, the capacitive effects are low and they are ignored. However, for better quality image reconstruction, the capacitive effect cannot be ignored. The cells have capacitive properties and capacitive leakage currents between cable shields might happen (Zimmermann et al., 2019). For creating images representing impedance (namely, capacitive and resistance reactance), it is necessary to measure variations in amplitude and difference of phase with EIT equipment. The phase and amplitude of every sinusoidal frequency component in the received signal are obtained by using a demodulator. The general application of the demodulator is to consider two signals, the first one is a sinusoidal signal with a predetermined frequency and the second one is a sinusoidal measured signal that has the impedance information and should demodulate.

EIT hardwares with bipolar current source usually use a Howland current source and a lagger circuit to produce 180^o delay. The active electrode can inject current at the electrode and simultaneously measure the potential at the electrode. This approach is called active electrode (Mellenthin et al., 2019). This research goes in the direction of incorporating a Howland current source to each electrode, this allows the generation of different types of current injection, including the trigonometric current injection (Gisser et al., 1987). This article explores the possibility of injecting current and measuring potentials using the same microcontroller. With this approach, the difference in phase between the generated and measured sinusoidal curves will have smaller errors. Other potential errors might appear, this research enumerates some of them.

This paper is structured as follows. Section 2 has the theoretical background. The Howland current source, the ADC and DAC converters, and the output impedance. Section refarchitecture explains the proposed architecture in which each electrode will have its own Howland current source. With this new architecture, the potential source

[1] e-mail: h.nasiri.ir@gmail.com.
[2] e-mail: rbenetti.eletronica@gmail.com.
[3] e-mail: takimotoyugo@gmail.com.
[4] e-mail: andrecavalheiro001@gmail.com.
[5] e-mail: guiduran@usp.br.
[6] e-mail: thiago@usp.br.
[7] e-mail: mtsuzuki@usp.br.

of error increases. Section 4 explains the demodulator. Section 5 has the experimental setup. Section 6 has the results and, finally, Section 7 has the conclusions and future works.

2. THEORETICAL BACKGROUND

The development of the EIT demodulator has some smaller modules: the Howland current source, the ADC, and DAC channels.

2.1 Howland Current Source

A voltage source is a device modelled as a voltage source in series with a resistance. In an ideal voltage source, this resistance is null ($R = 0$), while the real voltage source presents some resistance. For a current source, the device is modelled as a current source in parallel with a resistance. The ideal current source has an infinite resistance ($R = \infty$), while in practice there is a high-value resistance.

An ideal current source provides a constant current independent of the load connected to it. Considering an alternated current source, a sine function is used for the current, as $I = I_0 \sin(2\pi \cdot f \cdot t)$, where, f is frequency, t is time, I_0 is the amplitude of current. Usually, the operational amplifier presents the required characteristics to act nearly like an ideal current source because it has a high gain with high input impedance and low output impedance.

The Howland current source (see Fig. 1), invented by MIT's Prof. Bradford Howland in 1962, consists of an operational amplifier and a balanced resistor bridge to maintain the constant current value through the load even if the value of the load resistance changes. This circuit is a voltage-controlled current source that can provide high output impedance in a very wide frequency range. Considering an ideal operational amplifier, the impedance of this current source is infinite when the relationship

$$\frac{R_1}{R_2} = \frac{R_3}{R_4}$$

holds (see Fig. 1). In this balanced condition, the output current I_{out} is given by

$$I_{\text{out}} = \frac{+\text{Input}}{R_1}.$$

2.2 DAC and ADC channels

The DAC converts the digital signal into an analog signal according to the configured range and resolution. The full-scale voltage of the DAC is the maximum analog level that it can achieve. The DAC is characterized by its resolution, accuracy, and linearity. The accuracy can be analysed by comparing the actual output to the expected output, the linearity reflects an ideal DAC output. The resolution is achieved from

$$2^n - 1$$

where n is the number of bits.

The ADC converts analog signals into digital values. For a known sampling rate, the ADC samples an analog waveform at uniform time intervals and assigns a digital value to each sample.

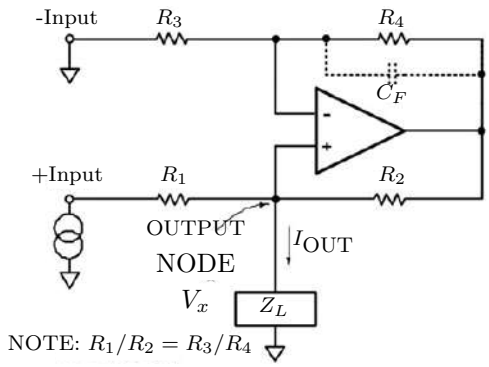

Fig. 1. Howland current source (Texas Instruments, 2008). The current source is the output node V_x where I_{out} is shown.

2.3 Output Impedance

The current source requires a high output impedance Z_0 in comparison with the load impedance Z_L. For an ideal current source, the output impedance Z_0 should be infinite. Even if the load impedance Z_L changes, the current on the load will be constant. The current on the load Z_L will stay in the range of b bits precision, when considering the ADC, it is required that the change i the current on the load Z_L be smaller than the least significant bit

$$Z_0 \geq (2^b - 1) \cdot Z_L^{\max},$$

where $Z_L^{\max}$ is the output with maximum load.

3. THE PROPOSED ARCHITECTURE

EIT hardware can have just one current source, this is called monopolar current source. They use just one Howland current source, and they are simple to calibrate. Usually, EIT hardware with bipolar current source can have one Howland current source and a lagger circuit to produce 180^o delay. Considering that l electrodes are used, these architecture of EIT hardware can acquire $l \times l$ measurements (Tavares et al., 2012, 2019).

This number of measurements is very small. It is possible to increase the measurements if different types of current injection are used (for example, different frequencies and the trigonometrical approach). This research goes in this direction, allocating one distinct Howland current source for each electrode. The calibration procedure will be much difficult when comparing with previous approaches.

Several errors exist when the measurements are performed (Martins et al., 2011, 2014). In this research, we enumerate some of the known problems: 1. Stability of the Howland current source when different loads are applied; 2. ADC and DAC resolution, precision, and linearity; 3. Sinusoidal curve acquisition delay.

4. THE DEMODULATOR

The demodulator determines the phase difference between the generated and the acquired sinusoidal curves. The initial time instant at which the sinusoidal curve is generated is known. Thus, the demodulator just considers that the

acquired data has known frequency and determines the delay. A general sine wave is represented by

$$f(x) = a \cdot \sin(b \cdot x + c) + d \quad (1)$$

where a is the amplitude, $b/2\pi$ is the sine wave frequency, c is the phase and d is the offset. In this research, we used a fitting algorithm which determines the parameters (a, b, c and d) values which will fit a given set of data. The fitting algorithm is based on the Gauss-Newton method (Kisabo et al., 2017).

Algorithm 1 Gauss-Newton method algorithm

```
Determine the initial guess and F
Calculate the Jacobian matrix J
i ← 0
while i ≤ N_max do
    if max_i(abs(t_i)) < ε then
        break
    t ← J^{-1}(−F)
    update current guess
    i ← i + 1
```

Algorithm 1 shows the fitting algorithm, which is based on the least-squares. The derivatives related to variables a, b, c and d are determined and they will compose the Jacobian matrix J which will guide the algorithm. Vector F is composed with the four parameters a, b, c and d. The algorithm depends on the initial guess, and for a better convergence it can be estimated from the acquired data. Considering that the frequency is known, the acquired data is separated in periods. The initial values for a and d can be estimated as

$$a = \frac{\max(V) - \min(V)}{2}$$

$$d = \frac{\max(V) + \min(V)}{2}$$

where $\max(V)$ and $\min(V)$ are the maximum and minimum values of the acquired signal in one period, respectively. The initial guesses of b and c are can be estimated by solving

$$t_{\max} \cdot b + c = \frac{\pi}{2}$$

$$t_{\min} \cdot b + c = \frac{3\pi}{2}$$

where $t_{\max}$ is the time at $\max(V)$ and $t_{\min}$ is the time at $\min(V)$.

5. EXPERIMENTAL SETUP

In this work, we used the FRDM-KL25Z development platform for the NXP MKL25Z128VLK4 microcontroller, which has integrated 16 bit analog-to-digital (ADC) and 12 bit digital-to-analog (DAC) converters. This evaluation board has a built-in debug interface for flash programming and is enabled for the ARM embed platform, which provides a C/C++ compiler. A periodic timer interrupt is used to activate the ADC and DAC to do their respective conversions.

Since the designed current source has some requirements, such as $2mA$ constant current for a variable load between $220\Omega \sim 1k\Omega$ and an excitation V_2 with amplitude voltage $3.3V$. The circuit response simulations were performed using LTSpice XVIII. To model the simulated circuit,

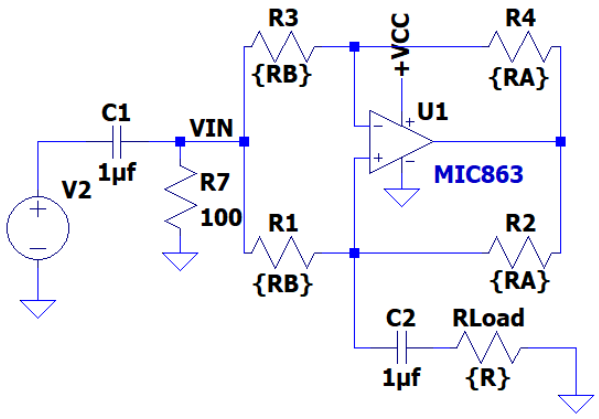

Fig. 2. Simulated Howland current source using LTSpice XVIII.

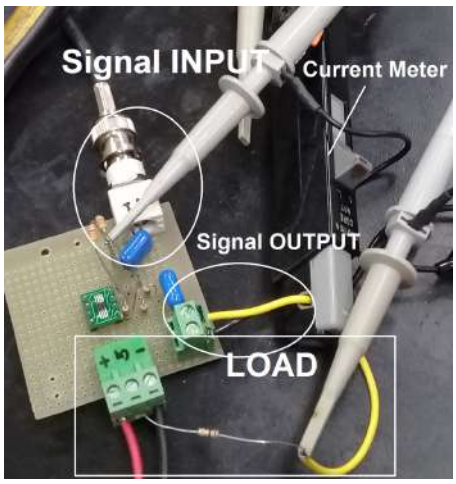

Fig. 3. Howland current source assembled hardware.

the CI MIC863 was used, with voltage source +VCC = $5V$. This component pack has two operational amplifiers where one of them was used with the resistors $R_A = [R2, R4] = 100k\Omega$, $R_B = [R1, R3] = 3,3k\Omega$ and $R_{\text{Load}} = [220, 550, 1k]\ \Omega$ (see Fig. 2). Input and output capacitors, and an input resistor R7 were included to remove DC components. Fig. 3 shows the assembled circuit.

6. RESULTS

The results are divided into three sections: 1. The Howland current source; 2. The ADC and DAC converters; and 3. The demodulator. The first section provides a comparison between the simulated circuit and the hardware experiment that will be used in the electrode. Adjustments were made in the simulated circuit and the experiments show if the results are coherent with the simulation results. The second section objective is to obtain the DAC and ADC characteristic curve and to establish the conversion limits for the electrode design. The last section shows the performance of the algorithm that will be used to demodulate the electrode signal.

6.1 Howland Current Source Tests

The simulation in the LTSpice XVIII was performed using three different loads: the minimum value is $R_{la} = 220\Omega$,

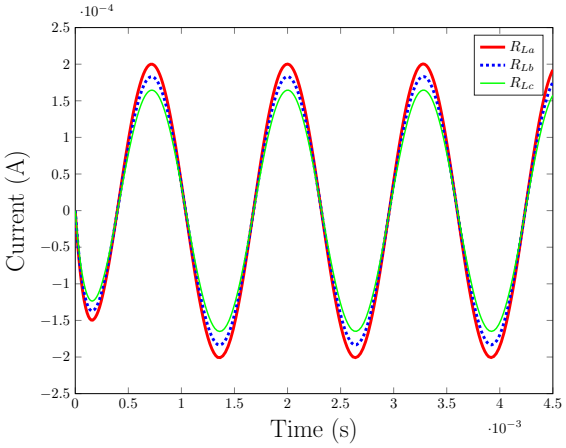

Fig. 4. Howland current source simulation response using LTSpice XVIII. The graphs show the current at the load R with different loads: $R_{La} = 220\Omega$, $R_{Lb} = 560\Omega$ and $R_{Lc} = 1k\Omega$.

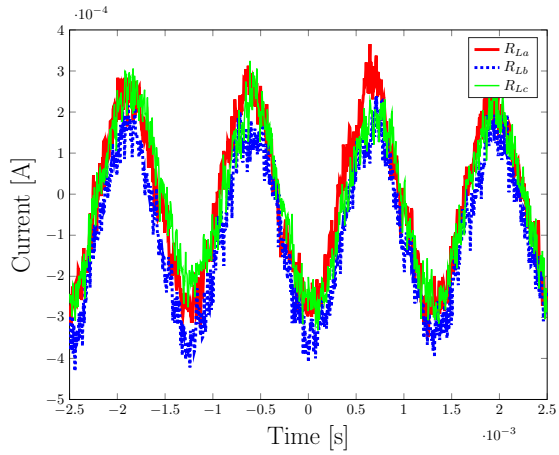

Fig. 5. Measured response using the physical circuit. The graphs show the current at the load R with different loads: $R_{La} = 220\Omega$, $R_{Lb} = 560\Omega$ and $R_{Lc} = 1k\Omega$.

medium value of $R_{lb} = 560\Omega$ and a maximum value of $R_{lc} = 1k\Omega$ (see Fig. 2). Fig. 4 shows the simulation results, and it is possible to observe variations of up to 25%, when the minimum and maximum loads are compared. The first amplitude has a different value because of the transient. Fig. 5 shows the resulting signal after assembling the circuit. In the real circuit, it is possible to verify that the operational amplifier output is not ideal and it has different capacitance for the offset and for the infinite resistance. The components must be precise, this is a difficult task when designing a Howland current source. We expect to improve the stability by comparing different operational amplifiers (Mahnam et al., 2016). It is also visible the presence of noise.

6.2 DAC and ADC Tests

For the FRDM-KL25Z, 12 bit DAC, measurements were made to verify the resolution, precision, and linearity of this DAC. The resolution of the DAC is expressed by $2^n - 1$, where n is the number of bits. For the chosen board the resolution is $4,095$, therefore it is possible to use values from 0 to $4,094$ to generate an analog wave.

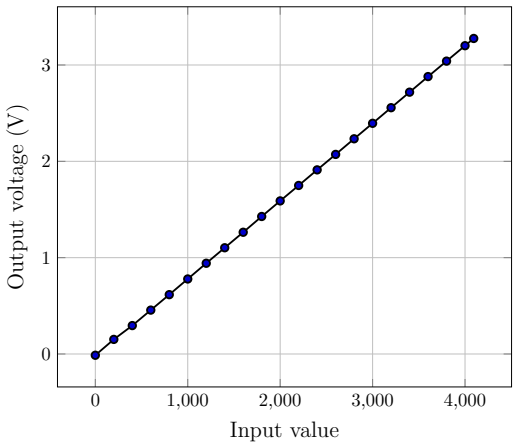

Fig. 6. The DAC linearity, it shows a good linearity.

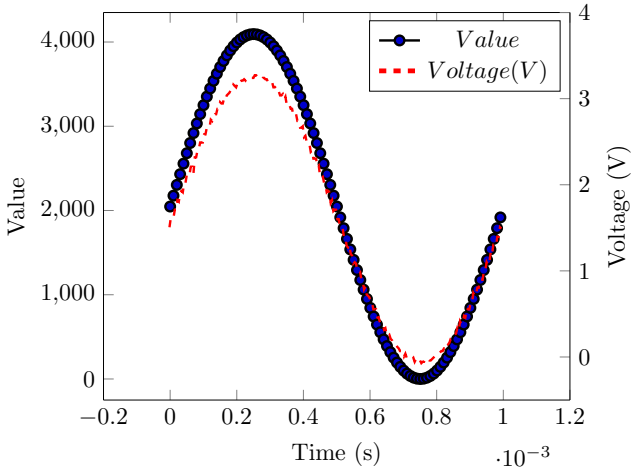

Fig. 7. Sine wave generated with 100 elements and oscilloscope measurements.

As for the precision, the oscilloscope was used to measure some values. Considering the minimum and maximum value, the DAC output was $-13.6\ mV$ with a standard deviation of 5 mV for the 0 value and the output was $3.2755\ V$ with a standard deviation of 3 mV for the $4,094$ value. From the measurements, it was possible to notice that the DAC presents an offset error of $-18.6\ mV$ and a standard deviation of 4 mV. The DAC linearity can be verified in Fig. 6. From the results, it was possible to notice a good linearity for the DAC module.

To test the board interruption limits to generate a sine wave, different values of interruption were used and the sine wave frequency was measured. The experiment showed that the minimum interruption to generate a sine wave is 10 μs. Fig. 7 shows the DAC input and the oscilloscope measurement using 100 elements. It is possible to notice that although the point density decreased, the measured voltage was approximately the same. Moreover, the graphs show a good correlation comparing the DAC input and the oscilloscope measurement. Table 1 shows the calculated frequency and the measured frequency considering different number of elements and interruptions.

The microcontroller MKL25Z128VLK4 comes with a 16 bits ADC, but for this experiment it was configured to use

Table 1. Sine wave frequency values. **Num** = Number of elements. **Int** = Configured interruption (mus). **Gen** = Generated frequency (Hz). **Meas** = Measured frequency (Hz)

Num	Int	Gen	Meas
100	10.013	998,70	996.02
100	19.931	501.73	502.51
50	10.013	1997.40	2,045.00
50	19.931	1003.46	1,004.00

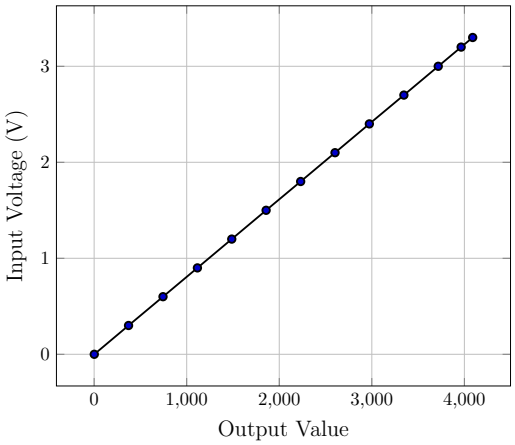

Fig. 8. ADC linearity, it is possible to observe a good linearity.

12 bits to interpret the analog signal. Since the V_{REFL} is 0 V and a V_{REFH} is 3.3 V for this microcontroller, the ADC has 2^{12} (4,096) values associated with the analog voltage range and the resolution is given by the following relationship

$$\text{Voltage Resolution} = \frac{V_{\text{REFH}} - V_{\text{REFL}}}{2^n}$$

where n is the number of bits used by the ADC. Then for this experiment, the minimum voltage variation that it is possible to read is 0.80 mV. As for the precision, a function generator was used to generate some DC values. Considering the microcontroller minimum V_{REFL} and maximum V_{REFH}, the ADC value detected for 0 V was 1.58 with a standard deviation of 1.6948 and the ADC value detected for 3.3 V was $4,089.6$ with a standard deviation of 3.6795. From the measurements, it was possible to notice that the ADC presents an offset error of 1 and a standard deviation of 4.3133. The ADC linearity can be verified in Fig. 8. From the results, it was possible to notice a good linearity for the ADC module.

To verify the ADC acquisition behaviour, a function generator with different values of frequencies was used in this experiment. The wave generated by the function generator was measured by an oscilloscope and the data was compared with the signal obtained by the ADC. Fig. 9 presents the acquisition of a 10 Hz sine wave using 100 samples and Fig. 10 presents the acquisition of a 40 Hz sine wave using 25 samples. From the graphs it was possible to notice a good correlation between the wave generated measured with the oscilloscope and the ADC output value.

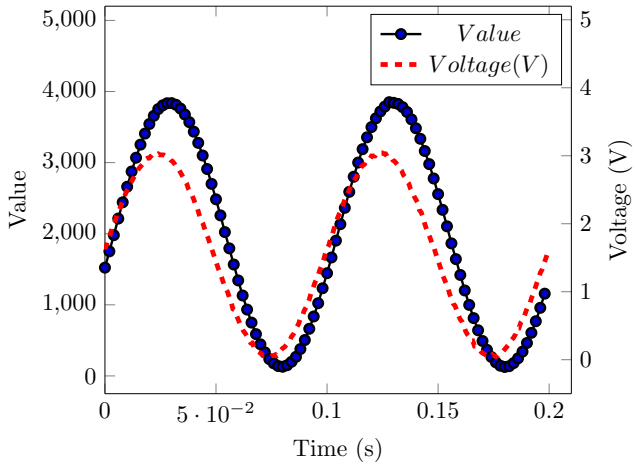

Fig. 9. Sine wave acquisition using 100 samples.

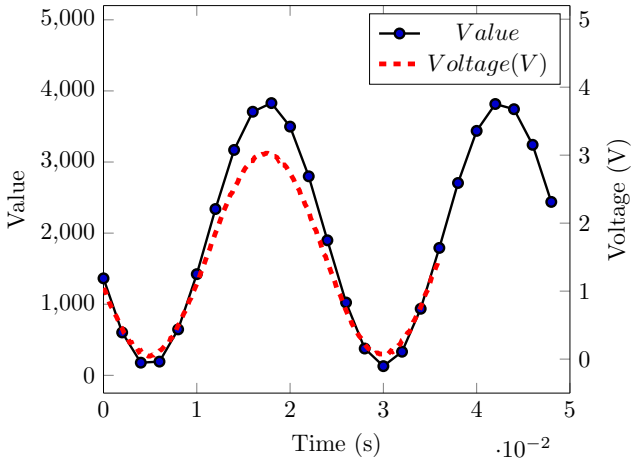

Fig. 10. Sine wave acquisition using 25 samples.

6.3 The Demodulator

To evaluate the Gauss Newton performance, the sampled data were converted into voltage values using the ADC linearity graph and the reconstructed sine wave parameters were compared with the configuration used in the function generator. The function generator uses the frequency, amplitude, and offset to generate the sine wave. For the Gauss Newton, the implementation provided the wave parameters using the sinusoidal form represented in (1). Table 2 shows the results of this comparison and Fig. 11 shows the graphs comparing the sampled data converted, the oscilloscope measurement and the Gauss-Newton approximation. It is possible to notice from the graph, a good phase approximation and the Gauss-Newton method has admissible precision when the number of samples decreases. For both cases, the convergence occurred in less than five iterations by considering the error 1, 0.1, and 0.01.

The demodulator considers $t = 0$ the initial time instant in which the microcontroller starts the sinusoidal curve generation. This way, the value of c is the difference in phase between the two sinusoidal curves.

Table 2. Gauss Newton Reconstructed Wave Parameters. **Num** = Number of Samples. **Func** = Function Generator Parameters. **Gauss** = Gauss Newton Parameters.**F** = Frequency (Hz). **A** = Amplitude (V). **O** = Offset (V).

Num	Func			Gauss		
	F	**A**	**O**	**F**	**A**	**O**
100	10	1.5	1.6	9.55	1.50	1.6
50	20	1.5	1.6	19.25	1.50	1.6
25	40	1.5	1.6	41.69	1.47	1.6

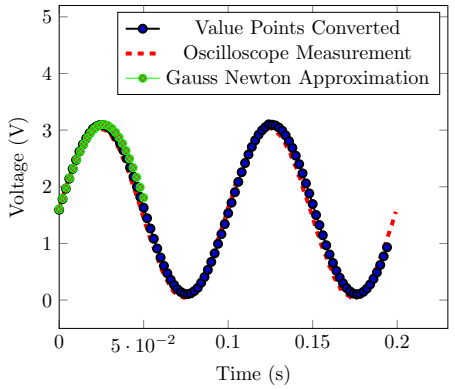

Fig. 11. Gauss Newton approximation for 100 samples.

7. CONCLUSIONS AND FUTURE WORKS

In this work, we tested the components required for an active electrode for demodulation. The comparison between the simulated and the real Howland current source circuit showed some small differences. They can be explained because the simulation considers an ideal operational amplifier. For the considered microcontroller, it was possible to observe that the DAC and ADC presented good linearity and precision. It was possible to reconstruct a sine wave using the Gauss-Newton algorithm even for a reduced number of samples. Moreover, the Gauss-Newton method shows that it is able to reach accurate and fast convergence even for small ϵ due to the good estimation of the initial guesses. Although it is possible to verify a good convergence of this iterative algorithm, further studies are required to verify if this algorithm can be used in an EIT application. Future works include the integration of all developed parts to construct the proposed new powerful architecture.

ACKNOWLEDGMENT

H. Nasiri and A. Cavalheiro are supported by FUSP/Petrobras. G. C. Duran and M. S. G. Tsuzuki are supported by CNPq (Grants 140.299/2020–3 and 311195/2019–9). The paper has the support from CAPES/PROAP - convênio 817.757/38.860.

REFERENCES

Bianchessi, A., Akamine, R.H., Duran, G.C., Tanabi, N., Sato, A.K., Martins, T.C., and Tsuzuki, M.S.G. (2020). Electrical impedance tomography image reconstruction based on neural networks. *IFAC-PapersOnLine*, 53(2), 15946–15951.

Gisser, D.G., Isaacson, D., and Newell, J.C. (1987). Current topics in impedance imaging. *Clin Phys Physiol M*, 8(4A), 39–46.

Kisabo, A.B., Uchenna, N.C., and Adebimpe, F.A. (2017). Newton's method for solving non-linear system of algebraic equations (NLSAEs) with Matlab/Simulink® and Maple®. *Am J Math Comput Model*, 2(4), 117–131.

Mahnam, A., Yazdanian, H., and Samani, M.M. (2016). Comprehensive study of Howland circuit with non-ideal components to design high performance current pumps. *Measurement*, 82, 94–104.

Martins, T.C., Camargo, E.D.L.B., Lima, R.G., Amato, M.B.P., and Tsuzuki, M.S.G. (2011). Electrical impedance tomography reconstruction through simulated annealing with incomplete evaluation of the objective function. In *33rd IEEE EBMS*, 7033–7036. Boston, USA.

Martins, T.C. and Tsuzuki, M.S.G. (2011). Simulated annealing with partial evaluation of objective function applied to electrical impedance tomography. *IFAC Proceedings Volumes*, 44(1), 4989–4994.

Martins, T.C. and Tsuzuki, M.S.G. (2012). Electrical impedance tomography reconstruction through simulated annealing with total least square error as objective function. In *34th IEEE EMBC*, 1518–1521. San Diego, USA.

Martins, T.C. and Tsuzuki, M.S.G. (2013). Electrical impedance tomography reconstruction through simulated annealing with multi-stage partially evaluated objective functions. In *35th IEEE EMBC*, 6425–6428. Osaka, Japan.

Martins, T.C. and Tsuzuki, M.S.G. (2015). EIT image regularization by a new multi-objective simulated annealing algorithm. In *Proc 37th IEEE EMBC*, 4069–4072. Milan, Italy.

Martins, T.C. and Tsuzuki, M.S.G. (2017). Investigating anisotropic EIT with simulated annealing. *IFAC-PapersOnLine*, 50(1), 9961–9966.

Martins, T.C., Fernandes, A.V., and Tsuzuki, M.S.G. (2014). Image reconstruction by electrical impedance tomography using multi-objective simulated annealing. In *IEEE 11th ISBI*, 185–188. Beijing, China.

Mellenthin, M.M., Mueller, J.L., Camargo, E.D.L.B., Moura, F.S., Santos, T.B.R., Lima, R.G., Hamilton, S.J., Muller, P.A., and Alsaker, M. (2019). The ACE1 electrical impedance tomography system for thoracic imaging. *IEEE T Instrum Meas*, 68(9), 3137–3150.

Tavares, R.S., Martins, T.C., and Tsuzuki, M.S.G. (2012). Electrical impedance tomography reconstruction through simulated annealing using a new outside-in heuristic and GPU parallelization. *J Phys Conf Ser*, 407, 012015.

Tavares, R.S., Sato, A.K., Martins, T.C., Lima, R.G., and Tsuzuki, M.S.G. (2019). GPU acceleration of absolute EIT image reconstruction using simulated annealing. *Biomed Signal Proces*, 52, 445–455.

Texas Instruments (2008). AN-1515 a comprehensive study of the Howland current pump. Version 1.0, Texas Instruments.

Zimmermann, E., Huisman, J.A., Mester, A., and Van Waasen, S. (2019). Correction of phase errors due to leakage currents in wideband EIT field measurements on soil and sediments. *Meas Sci Technol*, 30(8).